

Article

Sub-Annual Calving Front Migration, Area Change and Calving Rates from Swath Mode CryoSat-2 Altimetry, on Filchner-Ronne Ice Shelf, Antarctica

Jan Wuite ^{1,*} , Thomas Nagler ¹ , Noel Gourmelen ² , Maria Jose Escorihuela ³ ,
Anna E. Hogg ⁴  and Mark R. Drinkwater ⁵ 

¹ ENVEO—Environmental Earth Observation IT GmbH, A-6020 Innsbruck, Austria; thomas.nagler@enveo.at

² School of GeoSciences, Univ. of Edinburgh, Edinburgh EH8 9XP, UK; noel.gourmelen@ed.ac.uk

³ isardSAT, Parc Tecnològic Barcelona Activa, C/Marie Curie, 8-14, 08042 Barcelona, Spain; mj.escorihuela@isardSAT.cat

⁴ School of Earth and Environment, University of Leeds, Leeds LS2 9JT, UK; a.e.hogg@leeds.ac.uk

⁵ European Space Agency (ESA), ESTEC, 2201 AZ Noordwijk, The Netherlands; mark.drinkwater@esa.int

* Correspondence: jan.wuite@enveo.at; Tel.: +43-(0)512-319758-34

Received: 12 September 2019; Accepted: 19 November 2019; Published: 23 November 2019



Abstract: Mapping the time-variable calving front location (CFL) of Antarctic ice shelves is important for estimating the freshwater budget, as an indicator of changing ocean and structural conditions or as a precursor of dynamic instability. Here, we present a novel approach for deriving regular and consistent CFLs based on CryoSat-2 swath altimetry. The CFL detection is based on the premise that the shelf edge is usually characterized by a steep ice cliff, which is clearly resolved in the surface elevation data. Our method applies edge detection and vectorization of the sharp ice edge in gridded elevation data to generate vector shapefiles of the calving front. To show the feasibility of our approach, we derived a unique data set of ice-front positions for the Filchner-Ronne Ice Shelf (FRIS) between 2011 and 2018 at a 200 m spatial resolution and biannual temporal frequency. The observed CFLs compare well with independently derived ice front positions from Sentinel-1 Synthetic Aperture Radar imagery and are used to calculate area change, advance rates, and iceberg calving rates. We measure an area increase of $810 \pm 40 \text{ km}^2 \text{ a}^{-1}$ for FRIS and calving rates of $9 \pm 1 \text{ Gt a}^{-1}$ and $7 \pm 1 \text{ Gt a}^{-1}$ for the Filchner and Ronne Ice Shelves, respectively, which is an order of magnitude smaller than their steady-state calving flux. Our findings demonstrate that the “elevation-edge” method is complementary to standard CFL detection techniques. Although at a reduced spatial resolution and less suitable for smaller glaciers in steep terrain, it enables to provide CFLs at regular intervals and to fill existing gaps in time and space. Moreover, the method simultaneously provides ice thickness, required for mass budget calculation, and has a degree of automation which removes the need for heavy manual intervention. In the future, altimetry data has the potential to deliver a systematic and continuous record of change in ice shelf calving front positions around Antarctica. This will greatly benefit the investigation of environmental forcing on ice flow and terminus dynamics by providing a valuable climate data record and improving our knowledge of the constraints for calving models and ice shelf freshwater budget.

Keywords: Earth Observation; altimetry; calving front location (CFL); edge detection; CryoSat-2; swath processing; Antarctica; Filchner-Ronne Ice Shelf; iceberg calving

1. Introduction

The majority of the Antarctic coast is fringed by ice shelves that are formed from the floating extensions of outlet glaciers and ice streams mixed with marine accreted ice, snow and firn. The calving

front location (CFL) marks the seaward limit of the shelf, where the ice front meets the ocean. This edge is usually characterized by a steep ice cliff, often tens of meters high above the ocean surface, with the remaining ~90% of the ice shelf thickness concealed below. Its position is linked to climate and ocean forcing as well as internal ice dynamics and is subject to large fluctuations as the ice flows seaward, advancing the front, or as the ice front retreats following an iceberg breaking off. Iceberg calving from ice shelves, ice tongues and outlet glaciers is estimated to account for nearly half of the total volume of freshwater released from Antarctica [1,2], yet is difficult to quantify exactly due to incomplete or a lack of observations.

In recent years and decades, large calving events have reshaped the Antarctic coastline considerably. These include the calving of iceberg B-15 [3], the largest ever recorded, the calving of iceberg A-68 from Larsen-C in 2017 [4] and the disintegration of several ice shelves on the Antarctic Peninsula, such as Larsen-A and Larsen-B [5–7]. Calving, collapse and ungrounding of ice shelves from pinning points, i.e., rocky outcrops underneath the ice, can initiate a dynamic response that leads to increased ice export and sea level rise [8–13]. While large episodic calving events draw much scientific and public interest, smaller events often go unnoticed despite being an important component of the ice shelf cycle. From the ice velocity (V), ice thickness (H) at the calving front and a time sequence of CFLs, the iceberg calving rate can be computed. This can be used to estimate the background calving rate and total export of ice mass to the ocean. Therefore, monitoring the temporal evolution of the CFL is important, as a fundamental climate data record, indicator of changing boundary conditions or a precursor of dynamic imbalance. The CFL also serves as a practical boundary of the Antarctic coastal margin and is required as an input parameter for ice flow modelling, studies of calving processes and their driving forces, computing mass fluxes at the calving gate and ice shelf mass balance, as well as mapping glacier and ice shelf area change.

Baumhoer et al. [14] provides an overview of satellite sensors and existing methods used to detect Antarctic glacier and ice shelf front dynamics. Calving fronts of glaciers and ice shelves are in general mapped using Synthetic Aperture Radar (SAR) and optical satellite sensors [15,16]. These imaging instruments provide excellent spatial resolution for measuring the location of the ice edge, as the CFL can often clearly be discriminated due to marked differences in reflectance, spectral properties or texture of shelf ice and open water or sea ice. The use of active SAR is particularly valuable because it enables images to be acquired in all weather conditions and during the austral winter, when optical images would be obscured by clouds or have insufficient illumination. Furthermore, there is a stronger contrast between different types of ice (e.g., sea ice, fast ice and shelf ice) in SAR imagery, which are difficult to distinguish in optical imagery and allow ice shelf edges to be tracked more easily. To date, both manual and (semi-) automated techniques are applied to map CFLs in geocoded SAR and optical imagery, with manual delineation being the primary method. The automated approaches usually make use of some form of image segmentation followed by edge detection. More recently, advanced computer techniques have also been employed, including a method based on convolutional neural networks trained with manually determined calving fronts [17].

Several studies have extracted Antarctic-wide calving fronts and coastlines which are available through online data portals. The Scientific Committee on Antarctic Research (SCAR) Antarctic Digital Database (ADD) provides an Antarctic coastline, based on a variety of datasets, with sections occasionally updated. Liu and Jezek [18,19] and Jezek [20] used the 1997 and 2000 RADARSAT-1 mosaics to extract the entire coastline of Antarctica through a sequence of automated image processing techniques. Scambos et al. [21] also derived complete coastlines from MODIS-based mosaics of Antarctica (MOA) acquired in 2004, 2009 and 2014. The NASA Making Earth System Data Records for Use in Research (MEaSUREs) project also provided a coastline product for the entire Antarctic margin, including all ice shelves, derived from a variety of satellite radar interferometry data acquired during the International Polar Year (IPY 2007–2008) [2]. Other studies have provided coastlines for selected smaller study regions (for example, [22–25]). Baumhoer et al. [14] consolidated these existing CFL products to map and assess patterns of glacier and ice shelf front changes around Antarctica between

1972/1975 and 2009/2015. They reported difficulties caused by data gaps in time and space, differences in temporal sampling and the variety of different methods necessitating undesirable assumptions. The authors expressed the need for more homogenized data sets, with regular and more frequent mapping intervals, that would permit the use of dynamic calving fronts instead of the often-used steady-state ice fronts for mass balance estimates. They also noted the added value height information would provide for extracting ice front positions.

Currently the majority of the Antarctic coast is continuously covered by the Copernicus Sentinel-1 satellite mission at 6 to 12 day repeat intervals. Nevertheless, gaps in current and historical Earth observation coverage remain, CFLs are only available at relative moderate resolution or require a combination of different data sets making subsequent glaciological interpretation challenging. Moreover, SAR and optical images are subject to changes in radar backscatter or spectral reflectance, caused by for example ice melt or changing solar illumination, complicating automated approaches.

Here, we present a novel approach for CFL detection based on swath mode processed satellite radar altimetry data acquired by CryoSat-2 [26], between 2011 and 2018, which can fill existing temporal and spatial gaps, overcome some of the critical issues and meet some of the recommendations mentioned above. The method is also a new application for the CryoSat-2 mission that has not been previously exploited. The CFL detection is based on the premise that the ice edge is usually characterized by a steep cliff, with a steep drop of tens of meters towards the ocean surface or sea ice cover and which is clearly resolved in the elevation data. Our method, referred to here as the elevation-edge method, applies computational theory known as Canny edge detection and vectorization of the sharp ice edge in gridded elevation data for generating shapefiles of the CFL. Our main objective is to demonstrate the feasibility and added value of the approach. For this, we derived a contemporary update on calving front positions on the Filchner-Ronne Ice Shelf in East Antarctica allowing to measure change in ice shelf area and, in combination with ice shelf thickness measured from freeboard and ice velocity from Sentinel-1, iceberg calving rate between 2011 and 2018. The quality of the derived CFLs is assessed through intercomparison with manually derived CFLs from contemporaneously acquired SAR satellite data.

2. Study Region, Data and Methods

2.1. Study Region

We selected the Filchner-Ronne Ice Shelf (FRIS) situated in West Antarctica along the Weddell Sea coast to act as a regional case study to test our new method. With an area of approximately 430,000 km² FRIS is, by extent, the second largest ice shelf in Antarctica, after the Ross Ice Shelf. Together, it is estimated that they produce roughly a third of the total iceberg volume in Antarctica [1]. FRIS is fed by and modulates the flow of several major tributaries originating from both the East and West Antarctic Ice Sheets, including Evans, Rutford, Institute, Foundation, Support Force, Recovery and Slessor ice streams. Near the grounding line the ice thickness reaches well over 2000 m in some areas, making it, by volume, the largest floating ice mass in the world [27,28]. The ice shelf has a well-defined calving front characterised by a steep ice cliff more than 800 km long and split in two major sections by Berkner Island: the Ronne Ice Shelf (RON) and the Filchner Ice Shelf (FIL). Figure 1 provides an overview map of the study region, the hill-shaded background and grounding line are derived from CryoSat-2 data [29]. The calving front of RON is about 590 km long, with an ice thickness reaching a maximum of ~400 m downstream of Evans Ice Stream [27]. The calving front of FIL is about 230 km long with an ice thickness of well over 600 m near the centre. Flow velocity near the ice front on both RON and FIL varies between 2 m d⁻¹ near the shear margins and 4–4.5 m d⁻¹ in the centre of the ice shelf.

The last major calving event on FIL occurred in 1986, when icebergs A22–24, with a combined area totalling some 11,500 km², broke off [30]. Noteworthy events on RON occurred in 1998 and 2000, calving icebergs A-38/39 (8000 km²) and A-43/44 (11,500 km²) respectively [31]. Iceberg calving on RON is largely controlled by propagation of rifts originating from the Hemmen Ice Rise and d'Orville

Coast [32]. These long rifts are parallel to the ice front and eventually link with shorter perpendicular rifts [31]. Besides the occasional big events, it is unclear what the background calving rate and its variability or cyclicity is, as previous studies assumed steady-state front positions [1,2]. Comparing the CFL from the 1997 RADARSAT-1 mosaic [18–20] with one derived from recent Sentinel-1 imagery acquired in 2015 indicates that RON retreated by approximately 9 km near Cape Adams, and by more than 40 km near Hemmen Ice Rise, while FIL advanced by approximately 10 km at the margins and by more than 25 km near the central flow line (Figure 1).

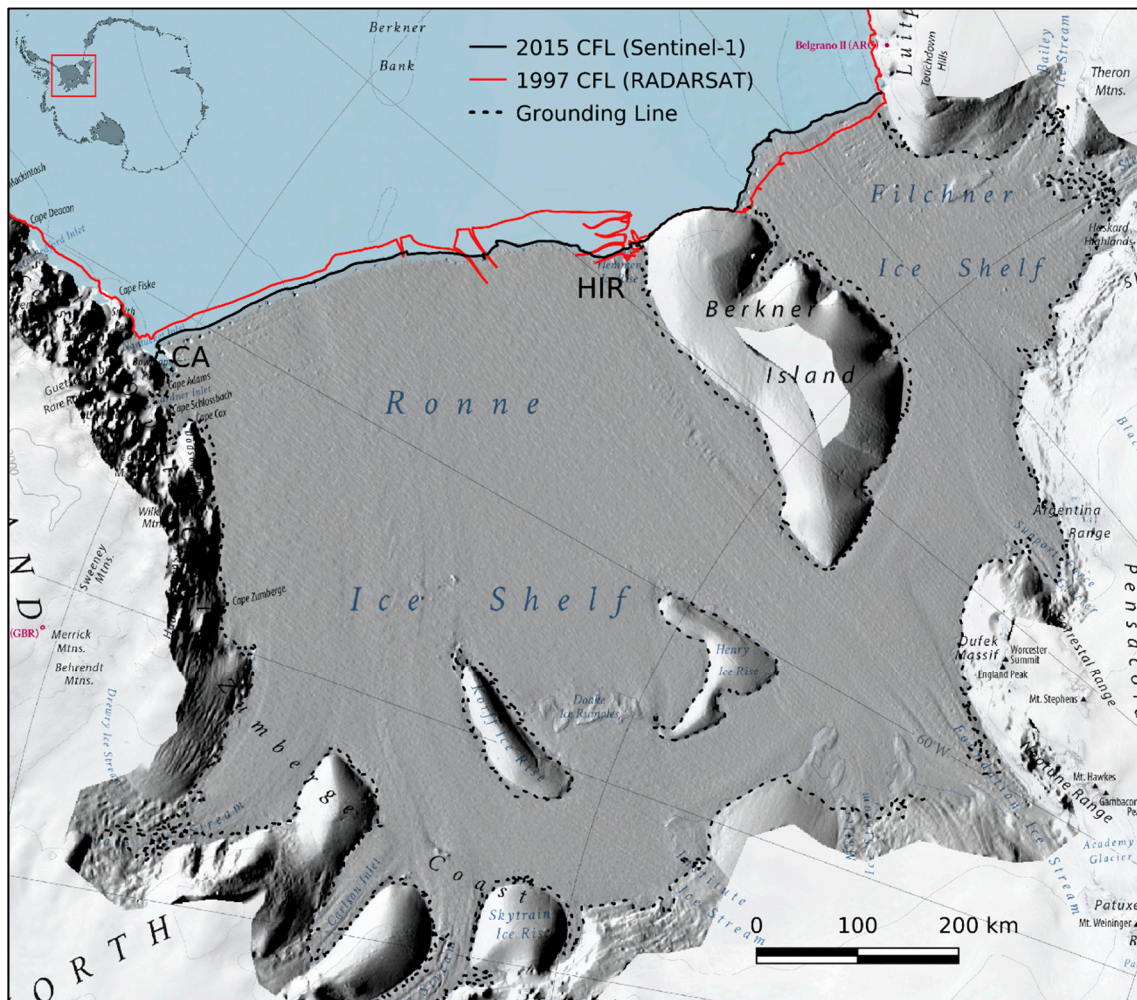


Figure 1. Hill-shaded relief map of the study region derived from CryoSat-2 (2017; see text), showing the location of the calving front in 1997 from RADARSAT-1 (solid red line [18,19]) and 2015 from Sentinel-1 (solid black line). The grounding line is indicated by the dashed black line [29]. CA = Cape Adams, HIR = Hemmen Ice Rise.

2.2. CryoSat-2 Data and Swath Mode Processing

We applied swath processing to data acquired between 2010 and 2018. We used the multi-looked echo (L1b product, baseline C) from the Synthetic Aperture Radar Interferometric (SARIn) mode of the SIRAL instrument on CryoSat-2 and applied the latest correction for platform attitude and roll bias [26]. The swath mode processing provides up to two orders of magnitude more surface elevation measurements when compared with the Level 2 point of closest approach (POCA) elevation measurements, with the same monthly sub-cycle [33]. The method requires waveform echoes with sufficient coherence and power to be selected [26]. Here, we chose a minimum coherence and power of 0.8 and -160 dB respectively. The phase was then unwrapped, and a global phase ambiguity resolved using an external digital elevation model (DEM) as described in [26], where the Reference Elevation

Model of Antarctica (REMA) provided at 8 m resolution was used [34]. A further data screening was then performed where outlier measurements, identified as deviating in height from the reference DEM by more than 100 m, were removed. The technique has been demonstrated to perform well over ice shelves despite relatively low surface slopes [35,36]. For additional details on the swath processing, we refer to Gourmelen et al. [26,35].

2.3. Delineating the Calving Front

In contrast to conventional CFL delineation methods, using SAR or optical imagery, we explore here the potential of using satellite radar altimetry elevation data as the primary input. To extract sub-annual CFLs, the swath data was first subdivided into biannual periods, covering March to August and September to February from 2011 to 2018 (corresponding to fall–winter and spring–summer seasons). The data acquired prior to 2011 was not used because of gaps over the ice shelf. We exploited the dense spatial sampling and repeat coverage of the swath mode elevation by gridding the data points for each interval to form DEMs with a uniform 200 m grid spacing in Antarctic polar stereographic projection. After initial outlier removal, based on a difference threshold (>50 m) with respect to the reference DEM, we applied minimum curvature interpolation (MCI) to rasterize the data [37]. The MCI method is computationally fast, but requires the selection of a suitable tension parameter, T , that can vary between 0 (minimum curvature solution) and 1 (harmonic surface). A tension parameter of $T = 0.5$ was selected as a good compromise providing a smooth overall appearance of the surface while preserving the edges. The gridded elevation data, which are given as ellipsoidal heights (WGS84), were converted to orthometric heights using a geoid derived from the GOCO05s satellite-only gravity field model [38]. Using the procedure described above, 15 elevation models were produced from the CryoSat-2 swath data with a regular temporal resolution of 6 months covering FRIS between 2011 and 2018. Figure 2 shows as example the DEM created for March–August 2017.

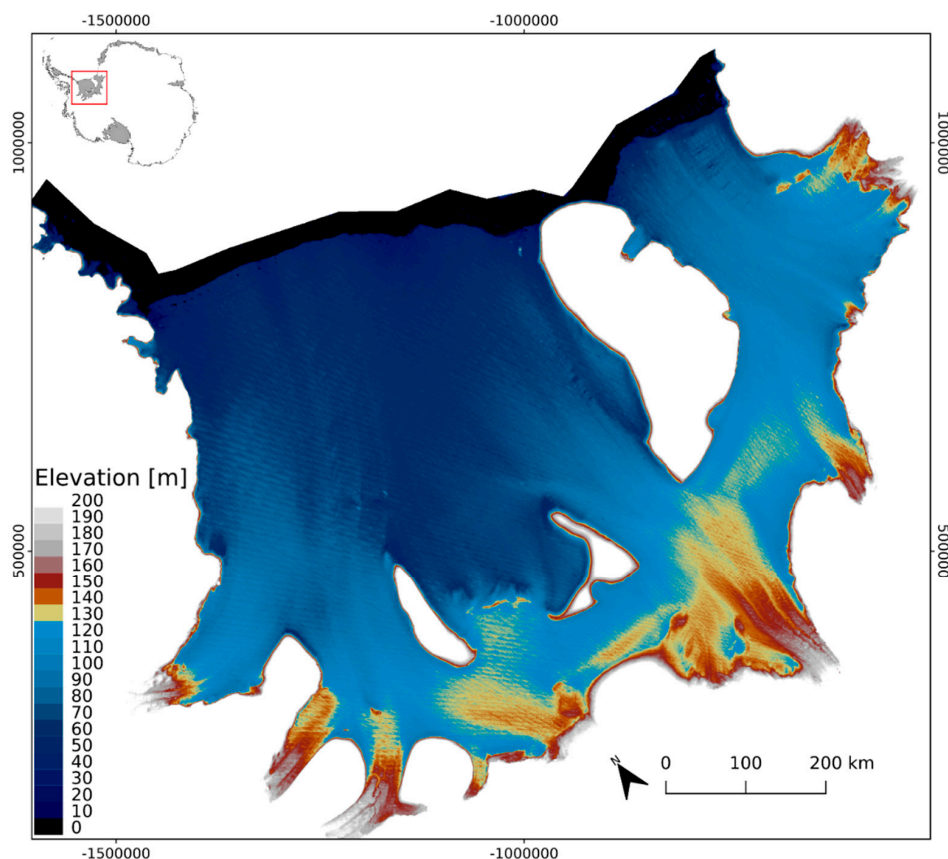


Figure 2. Digital elevation model (DEM) of the Filchner-Ronne Ice Shelf derived from CryoSat-2 swath altimetry data acquired between March and August 2017. Projection is Antarctic Polar Stereographic.

Subsequently, the CryoSat-2 swath DEMs were used as input to extract and vectorize the CFLs automatically applying a Canny edge detection algorithm [39]. The Canny edge detector is a multi-stage edge detector that first applies a Gaussian filter to reduce noise and subsequently computes the intensity of gradients in two dimensions. Discontinuities, e.g., potential edges, are thinned and selected using hysteresis thresholding. Liu and Jezek [18,19] and Krieger and Floricioiu [16] also applied Canny edge detection for derivation of CFLs from SAR images of Antarctica and Greenland respectively. We applied a 5×5 Gaussian kernel and a lower and upper threshold of 5 and 20 respectively, which resulted in a continuous and realistic CFL. For more complex calving fronts, with many rifts or an iceberg mélange, additional segmentation steps are mandatory. In a final step, the results were vectorized, converted to shapefiles and manually checked and cleaned if required.

The CryoSat-2 swath DEM generation as well as the CFL processing, vectorization and visualisation, as shown in the simplified flow diagram (Figure 3) is highly automated and done using existing open source software and routines, including Generic Mapping Tools (GMT), Python, SciPy, GDAL, GRASS and QGIS. The 15 derived CFL and DEM products form the primary input data for subsequent glaciological analysis.

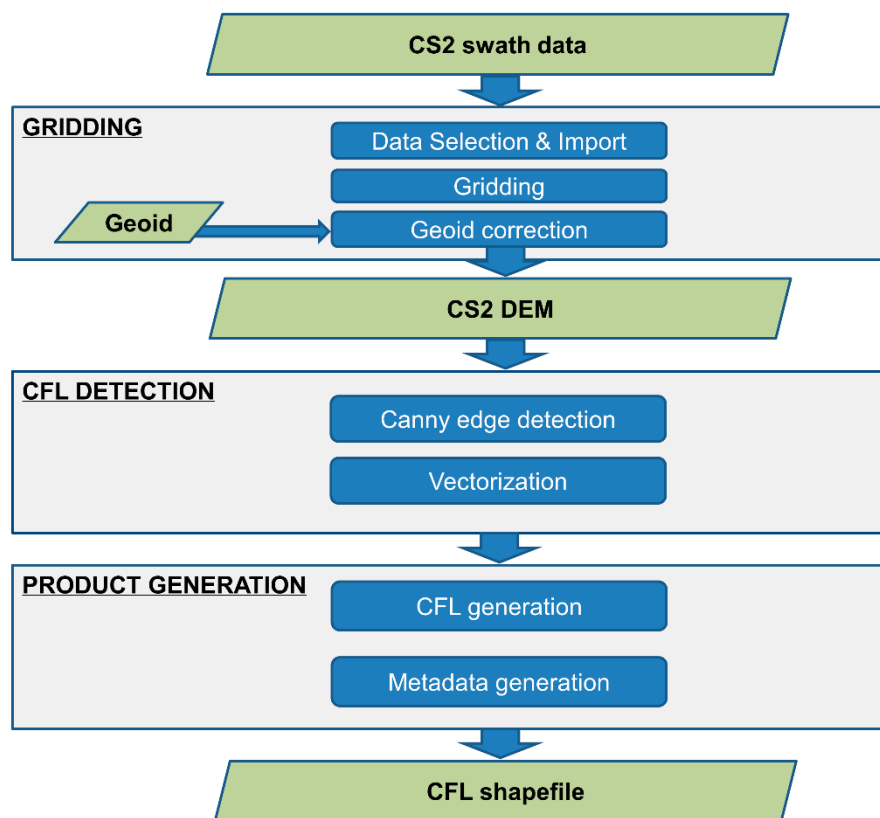


Figure 3. Processing chain for deriving a calving front shapefile from CryoSat-2 swath data.

2.4. Area Change and Iceberg Calving Rate

We used the CFL time series to calculate calving front migration, area change and iceberg calving rate of RON and FIL averaged from 2011 to 2018 (6.5 years). The iceberg calving rate (u_c) is the amount of ice breaking off at the ice front per unit time and unit vertical area [40] and can be expressed as the difference between the velocity at the ice front, v_f , and the rate of change (advance or retreat) in terminus position, L [41]

$$u_c = v_f - \frac{dL}{dt} \quad (1)$$

If the ice velocity at the ice front is larger than the calving rate the ice front advances. Retreat occurs when the calving rate is greater than the terminus velocity. dL can be determined from the ice front position at two different epochs. Frequently, width-averaged values are used, which is often suitable for smaller tide-water glaciers, but less so for large ice shelves. Here, we exploit our data set of ice front positions to account for lateral variations in the calving rate and calculate the iceberg calving rate (expressed as mass) using a simple approach which combines the CFL time series and ice thickness, based on [42]

$$u_c = \left(\frac{A_{nc} - A_{ac}}{dt} \right) H_i \rho_i \quad (2)$$

where A_{ac} is the actual area change, calculated from the enclosed polygon formed by intersecting the (line) shapefiles of the observed 2011 and 2018 CFLs in a GIS, and A_{nc} is the area change for the case where no calving has occurred. The difference between these two provides the total area of ice loss. H_i is the mean effective ice thickness of the calved area, ρ_i the density of ice (917 kg m^{-3}) and dt the time difference.

To obtain the ice shelf area change without calving, A_{nc} , we approximate the configuration of the CFL in 2018 through extrapolation of the observed 2011 CFL using an ice velocity map. To do this, we calculate the displacement Δx of evenly spaced points, 200 m apart, along the 2011 calving front in the direction of ice flow (i.e., the particle flow path) by integrating the local velocity v_i over time

$$\Delta x = \int_{t1}^{t2} v_i(t) dt \quad (3)$$

The ice velocity is obtained from repeat-pass Sentinel-1 Interferometric Wide swath mode (IW) data acquired between 2014 and 2018. These data have been used to compile a mean ice velocity map, gridded at 200 m pixel spacing, using iterative offset tracking [43]. The displacement is calculated for each point along the calving front. By connecting the projected points, a new imaginary calving front is formed, which approximates the configuration of the ice shelf calving front in 2018 if no iceberg calving would have occurred. The total area of ice lost due to calving is then simply computed from the area difference of the enclosed polygons representing the projected area change (without calving) and the actual area change since 2011. The extrapolation approach assumes no major change in flow velocity or direction at the ice front, which is a plausible assumption as velocity gradients are usually very small near the front of a floating ice shelf.

The total calved area is converted to volume and mass loss rate by deducing the ice thickness from the height above flotation, assuming the ice is freely floating which is usually the case near the ice front. For this, the DEMs are combined with long-term (1980–2013) averaged estimates of firn air content from the 27 km regional atmospheric climate model RACMO2/ANT [44] that we resample to the same grid spacing. The effective ice thickness, H_i , is derived from ice shelf freeboard following Van den Broeke et al. [45] and Chuter and Bamber [27]:

$$H_i = \frac{(h_{asl} - \Delta h) \rho_{sw}}{\rho_{sw} - \rho_i} \quad (4)$$

where h_{asl} is the surface elevation above mean sea level, ρ_i is the mean density of pure ice (917 kg m^{-3}), ρ_{sw} is the mean density of seawater (1027 kg m^{-3}) and Δh is the firn depth correction which is derived from a firn densification model. Typical values for Δh on FRIS are between 15 and 20 m.

3. Results

3.1. Calving Front Migration

An examination of the CryoSat-2 swath DEMs (Section 2.3), reveals pronounced surface undulations on the ice shelf with higher elevations (i.e., thicker ice) along ice stream flow paths, along with large crevasses and rifts in the ice. The CFL is clearly resolved by a sudden drop in the surface elevation of tens of meters at the ice front, in some places 40 m to 50 m, as the ice shelf meets the ocean surface. The temporal evolution of the CFL and large crevasses can clearly be tracked in the CryoSat-2 swath DEMs.

The elevation-edge CFL product results in a sequence of uninterrupted vector lines along the entire margin of FIL and RON (Figures 4 and 5), clearly revealing the change in ice front position throughout the biannual time series. Along the majority of the ice front the vector lines are quasi-parallel and show a gradual advance during the observation period. This confirms that we are tracking the ice front, and also implies that over these short timescales the calving rate along the margin is in general lower than the advance rate, which is the dominant signal. Of particular interest is a section on the western side of FIL, where some of the CFLs are overlapping. In this location a calving event occurred in the period September–February 2012–2013. Looking in closer detail reveals additional but smaller scale calving events along the entire ice front throughout the study epoch.

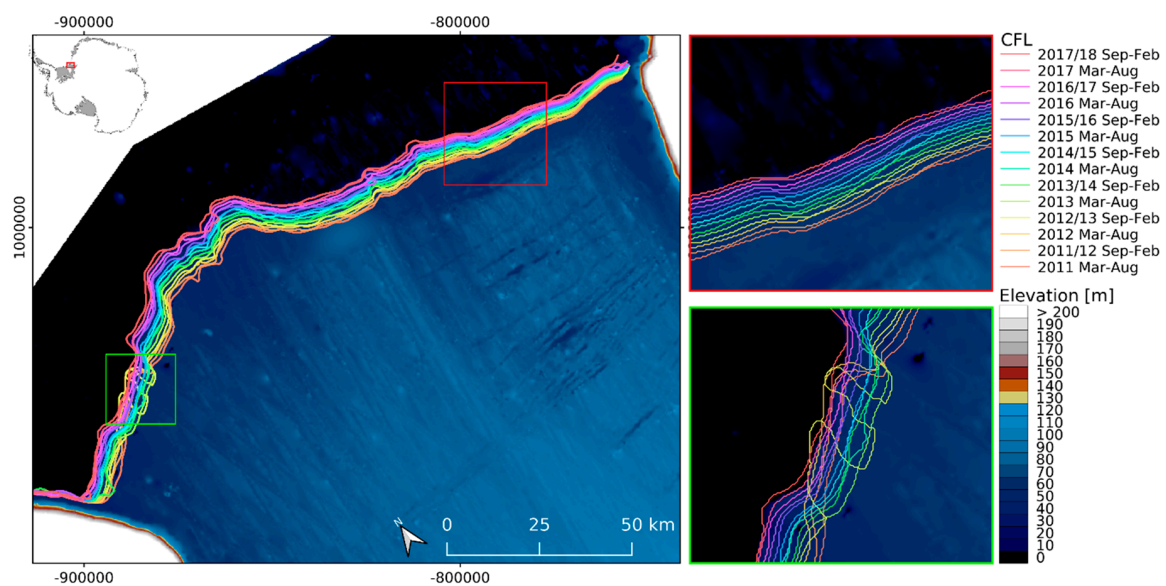


Figure 4. Biannual CFL time series for Filchner Ice Shelf (FIL) derived from CryoSat-2 swath altimetry (background CryoSat-2 swath DEM). The red square shows area of detail shown in the upper right panel; the green square shows area of detail shown in the lower right panel, where a larger calving event occurred in 2012–2013 (see Section 3.3). Projection is Antarctic Polar Stereographic.

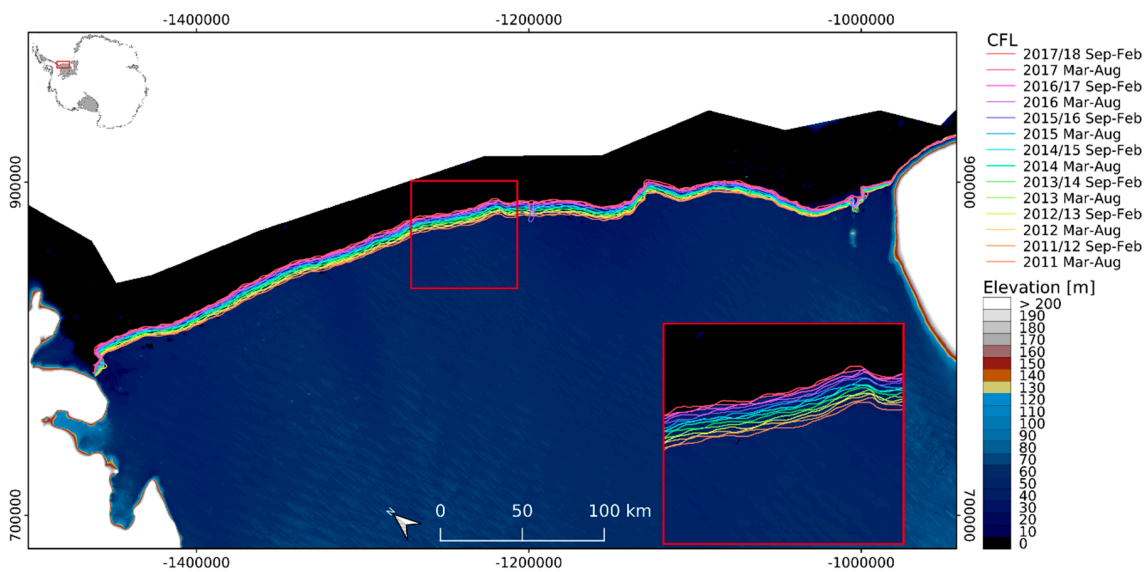


Figure 5. Biannual calving front location (CFL) time series for the Ronne Ice Shelf (RON) derived from CryoSat-2 swath altimetry (background CryoSat-2 swath DEM). Inset shows close-up of area outlined by the red square. Projection is Antarctic Polar Stereographic.

Based on the total advance between March and August 2011 and September and February 2017–2018, we calculated average advance rates for both ice shelf sections along flow lines (Figures 6 and 7). The advance rate on RON varies along the ice front and ranges between 0.38 km a^{-1} and 1.57 km a^{-1} , with the highest advance rates in the centre of the ice shelf and smaller advance rates near the margins. On FIL, we find nearly equivalent advance rates ranging between 0.42 km a^{-1} and 1.73 km a^{-1} with maximum advance rates found just left of the centre. Apart from one isolated large calving event on the Filchner IS, and disruption to the calving position seaward of the Hemmen Ice Rise on the Ronne IS, no major retreat in the calving front was measured throughout the whole 6.5 years long study period.

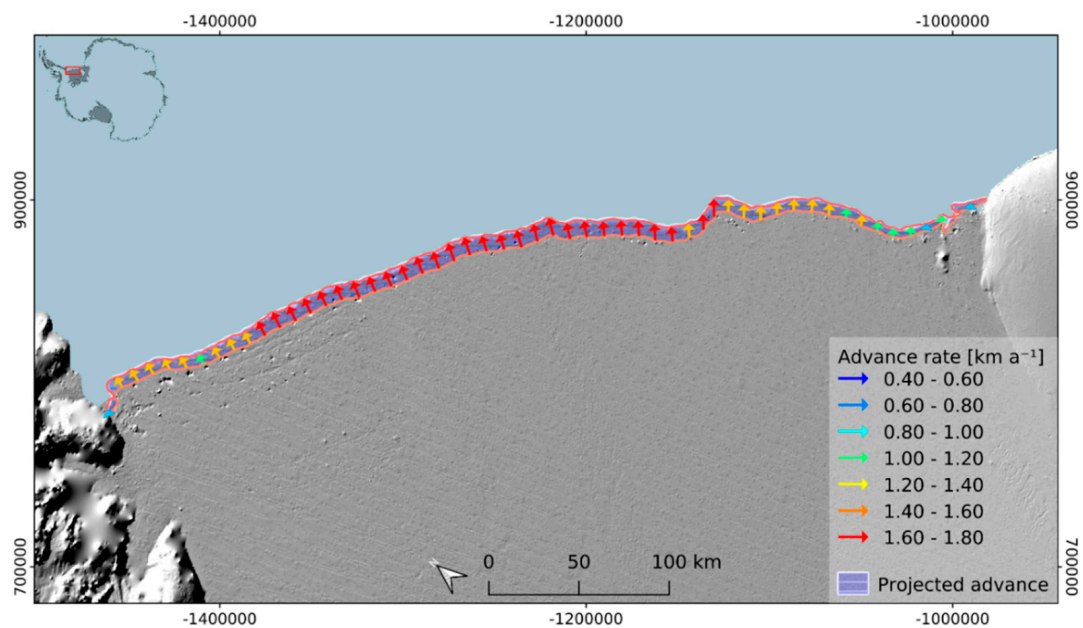


Figure 6. Ice front advance rate and projected advance between 2011 and 2018 for RON. Projection is Antarctic Polar Stereographic.

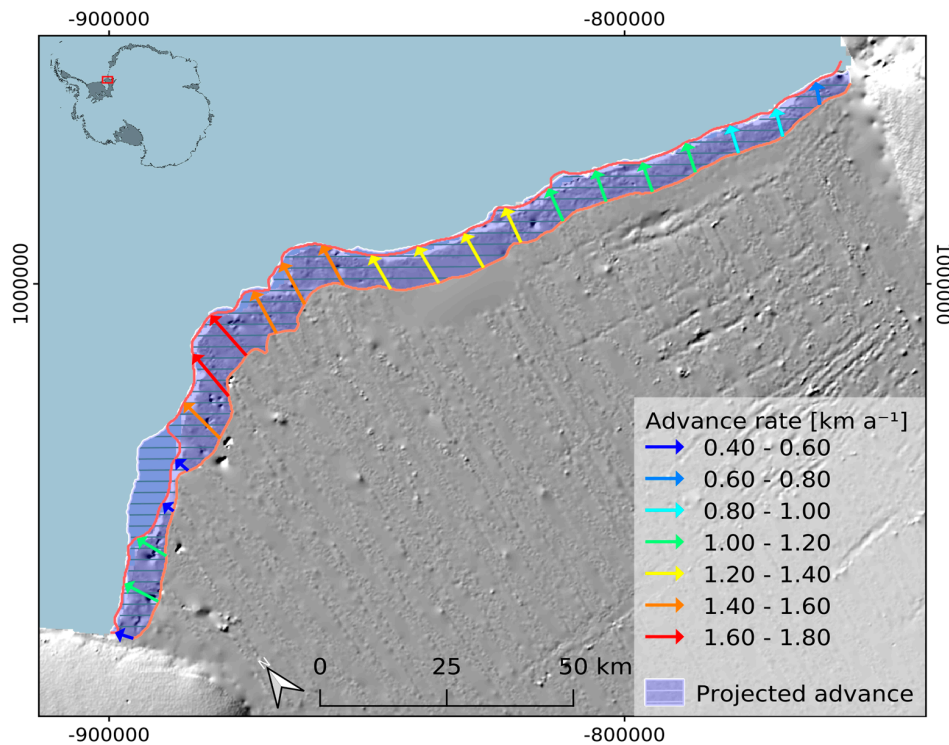


Figure 7. Ice front advance rate and projected advance between 2011 and 2018 for FIL. Projection is Antarctic Polar Stereographic.

3.2. Intercomparison with Manually Derived CFLs from Sentinel-1

To confirm the elevation-edge CFL detection approach, we validated our method with manually delineated ice fronts measured from a geocoded Sentinel-1 image. In June 2015 Sentinel-1A acquired several tracks covering the entire FRIS ice front in IWS mode. We processed and geocoded a SAR image acquired on 6 June, 2015, which roughly centres on the CFL for March–August 2015. Figure 8 shows the SAR image along with the CFLs derived from CryoSat-2 and Sentinel-1. As can be seen, the CFL derived from the CryoSat-2 DEM shows a very good overall agreement with Sentinel-1, confirming that we are tracking the ice edge and illustrating the robustness of the results. Along, most of the ice edge the deviation between the two CFLs is in the order of two or three grid cells (400–600 m), but in a few cases, larger deviations (>1000 m) exist. The intercomparison is useful to detect any obvious systematic discrepancies but the interpretation is complicated. The main complicating factor is due to differences in the temporal resolution. The CFLs derived from SAR imagery are fixed for a particular date, while the CFLs derived in this study are based on data accumulated over a time span of six months. Calving events which occur within this time period may not be so well resolved as they will be averaged into the DEM, therefore an exact agreement may not be expected.

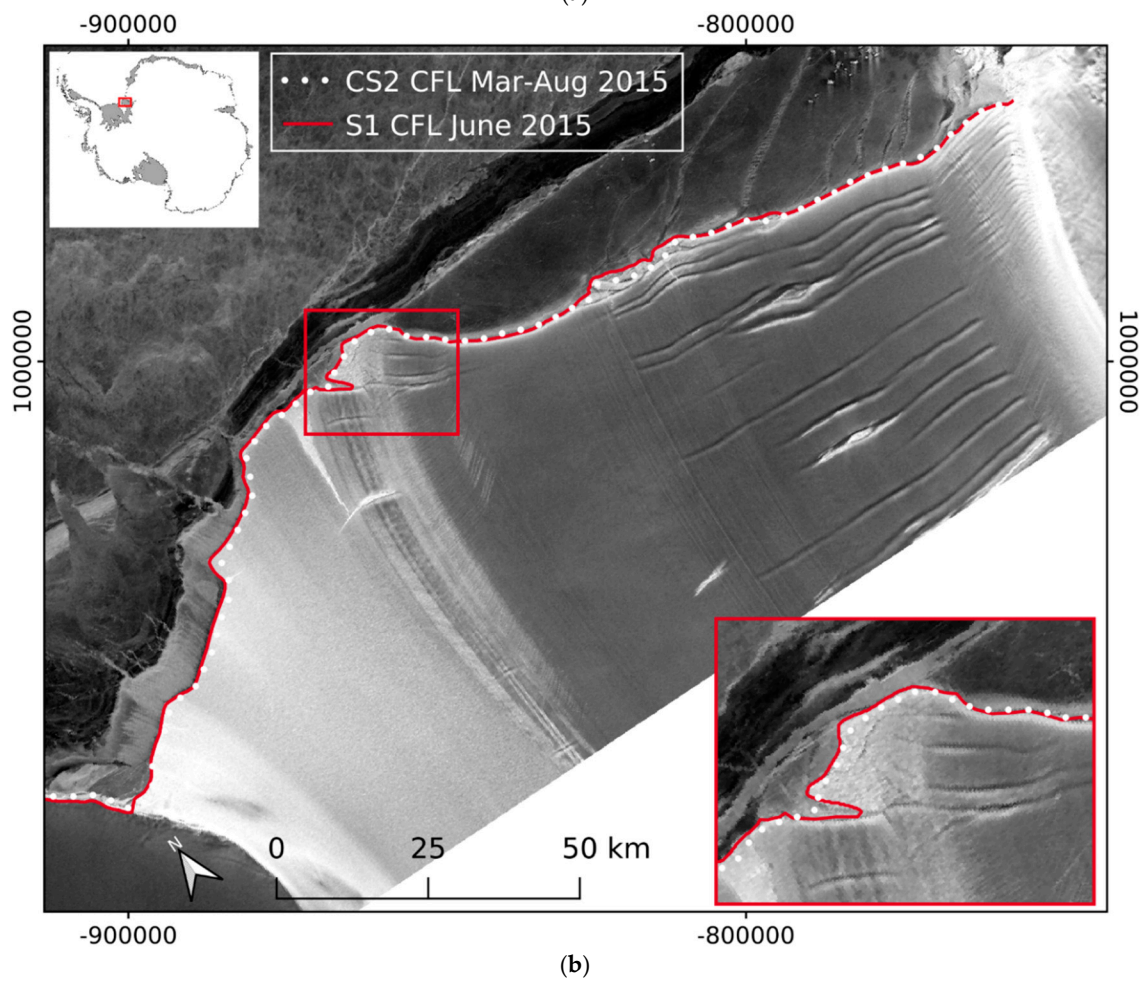
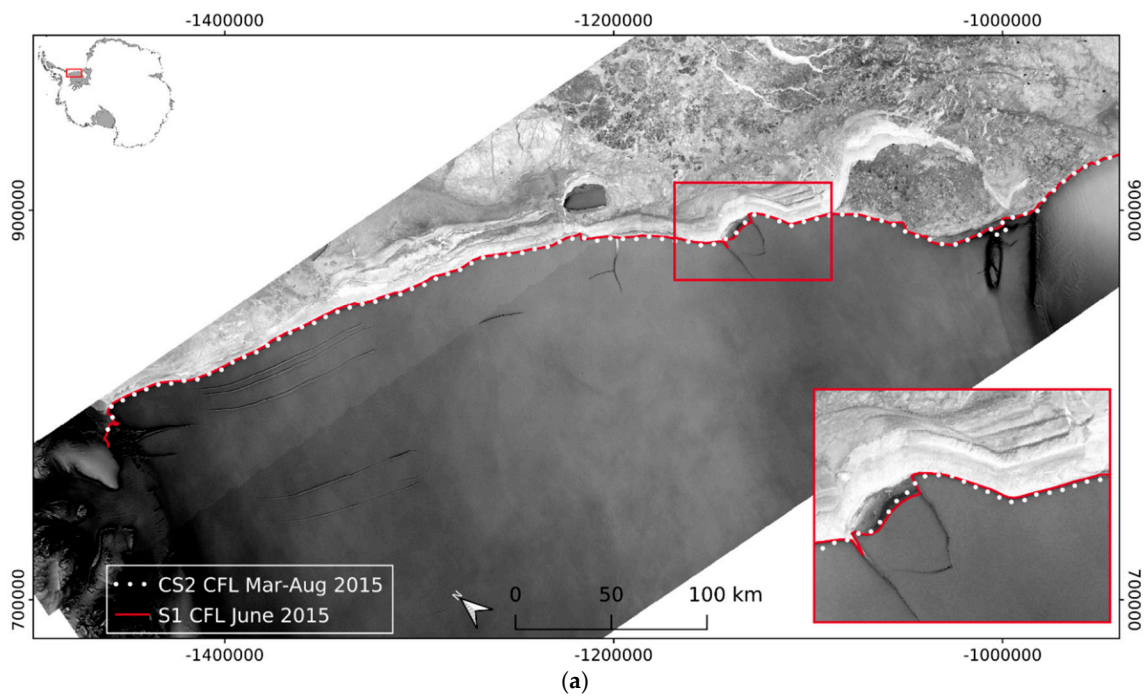


Figure 8. The CryoSat (CS2) CFL results show good agreement with manually derived CFLs using Sentinel-1 (S1) imagery (acquired on 6 June, 2015), (a) Ronne Ice Shelf; (b) Filchner Ice Shelf.

3.3. Area Change and Iceberg Calving Rate Results

Figure 9 illustrates the calving of an iceberg, detected by our elevation-edge method and also captured in a cloud-free Landsat-7 image (courtesy of the U.S. Geological Survey), which occurred in November 2012 on the Filchner Ice Shelf. The Landsat image was acquired on 23 November 2012 and clearly shows the iceberg just after it broke off. The outline/area of the iceberg in the Landsat image (123 km²) agrees very well with our findings (118 km²), with less than 5% difference in area estimate. The good agreement confirms the validity and the high accuracy of our approach and the ability to detect calving events at a sub-annual temporal resolution.

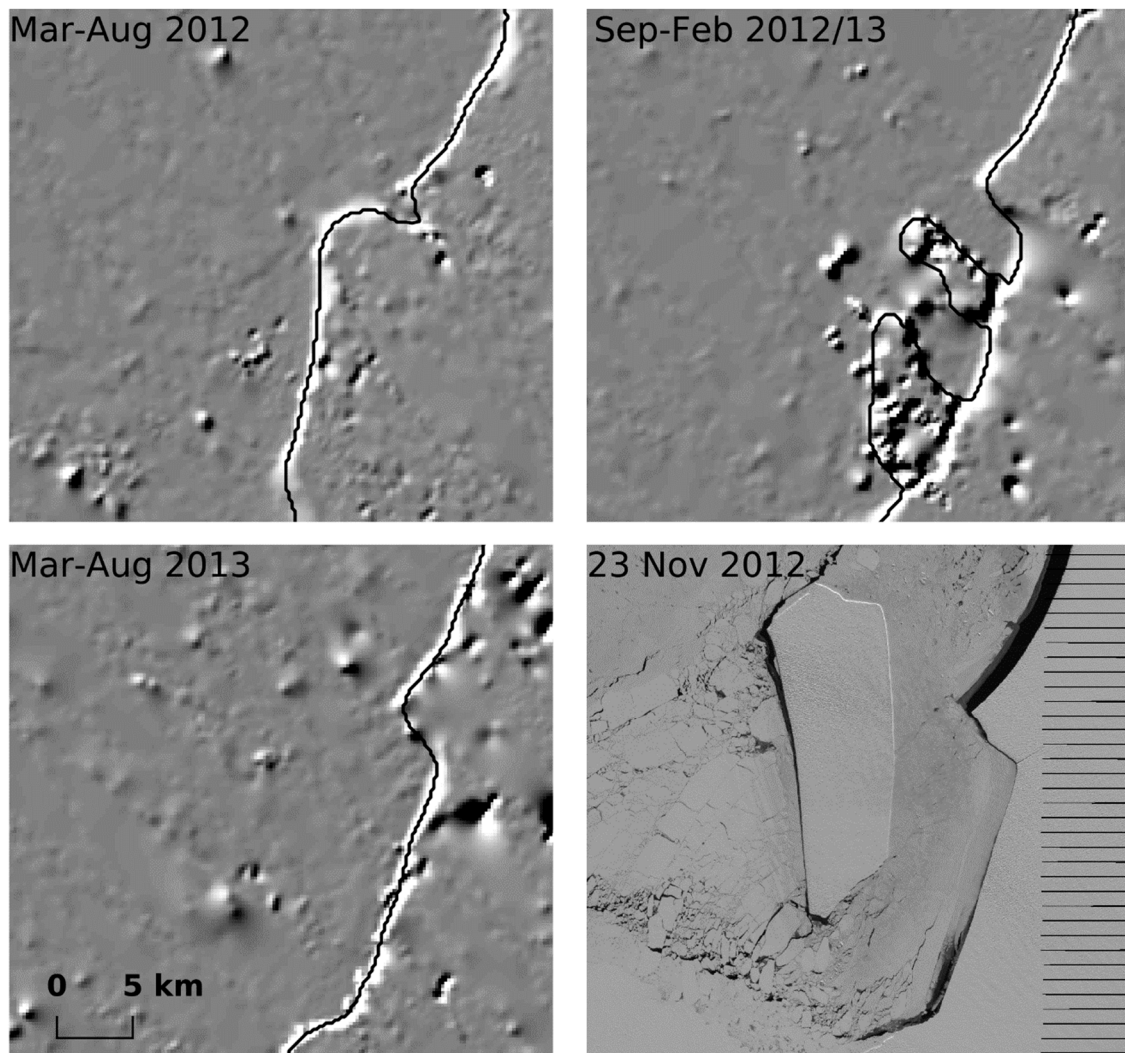


Figure 9. Detail of the calving front of the Filchner Ice Shelf (see the green box in Figure 4) illustrating the calving of an iceberg in November 2012. Depicted are the calving fronts in March–August 2012 (**top left**), September–February 2012–2013 (**top right**), March–August 2013 (**bottom left**), background hill-shaded swath DEMs. Also depicted is a Landsat-7 image (USGS) acquired on 23 November 2012, clearly showing the iceberg just after it calved. (**bottom right**).

As a further practical application of the derived calving front positions, we calculated total area change and iceberg calving rates observed between 2011 and 2018 (Section 2.4). We find a total area increase of $5263 \pm 263 \text{ km}^2$ ($\sim 810 \pm 40 \text{ km}^2 \text{ a}^{-1}$) for FRIS between March–August 2011 and September–February 2017–2018.

For FIL the total observed ice shelf area increase is 1449 km², while the projected area increase (see Figure 7), i.e., without calving, amounts to 1604 km². The calved ice area is therefore calculated to

be $155 \pm 8 \text{ km}^2$ (allowing 5% uncertainty). The one major iceberg calving event we observed resulted in a loss of approximately 105 km^2 of ice, suggesting that most calving can be attributed to infrequent larger iceberg calving events. With an average ice thickness of $418 \pm 21 \text{ m}$ along the calving front, this translates to a volume loss of about $65 \pm 5 \text{ km}^3$ or roughly $59 \pm 4 \text{ Gt}$ of ice mass through iceberg calving. The mean calving rate on the Filchner Ice Shelf for the 6.5 year study period based on this is $9 \pm 1 \text{ Gt a}^{-1}$, which represents $\sim 10\%$ of the steady-state calving flux, i.e., the calving flux required to maintain a steady-state ice front, which is $95 \pm 7 \text{ Gt a}^{-1}$ for the same period.

Applying the same method for RON, we measure a total area increase of 3814 km^2 , whereas the projected area increase (see Figure 6) without calving is 4048 km^2 . The calved ice area of the Ronne Ice Shelf is therefore $234 \pm 12 \text{ km}^2$, which is slightly higher than for FIL, but due to a much lower average ice thickness of $222 \pm 11 \text{ m}$, this translates to a lower volume loss of about $52 \pm 4 \text{ km}^3$ and a mass loss of $48 \pm 3 \text{ Gt}$ of ice. This is equivalent to $\sim 80\%$ of that observed on FIL. The mean calving rate observed on RON is $7 \pm 1 \text{ Gt a}^{-1}$, which represents only $\sim 6\%$ of the steady-state calving flux ($127 \pm 9 \text{ Gt a}^{-1}$) for the same period.

4. Discussion

The Antarctic Ice Sheet has been portrayed as a barometer of climate change and is currently losing mass at an accelerating rate, and is expected to do so in the future, with significant implications for global sea-level rise [46,47]. In order to accurately determine the future response of the Antarctic ice sheet to ongoing climate warming it is essential to quantify the major components of current mass loss and understand their principal drivers. Antarctic ice is primarily drained through the peripheral ice shelves surrounding most of the continent. Although these floating ice shelves do not contribute directly to sea-level rise, they play a critical role in providing resistance to flow from upstream grounded ice [8–13]. It is therefore essential to accurately determine their mass budget. The iceberg calving rate forms a key element of the ice shelf mass budget, which is traditionally determined from estimates of the surface mass balance (net snow accumulation), basal melting and the mass flux divergence. The latter being determined from the ice flux at the grounding line (total solid ice inflow) and at the ice front (total solid ice outflow), based on measurements of ice thickness and ice velocity. In absence of detailed knowledge on the exact position of the calving front previous studies have relied on the steady-state calving approach as a proxy for iceberg calving, assuming a fixed position of the ice front [1,2].

The combined steady-state calving flux calculated for RON and FIS between 2011 and 2018 is $222 \pm 11 \text{ Gt a}^{-1}$, which compares well with previous estimates of $212 \pm 17 \text{ Gt a}^{-1}$ by Liu et al. [41] for the period 2005–2011 and $221 \pm 26 \text{ Gt a}^{-1}$ by Rignot et al. [2] for the period 2007–2008. Previous estimates of freshwater flux from FRIS have assumed these steady-state calving rates alone because time-dependant calving data were unavailable, thereby ignoring any changes in areal extent of the ice shelf. We show that such approach for 2011–2018 would overestimate the freshwater budget from FRIS by 206 Gt of ice or 224 km^3 of freshwater every year. This example serves to illustrate that the steady front flux can be very different than the actual iceberg calving flux, particularly on sub-decadal time scales, and that CFLs should start to be more routinely monitored.

The observed CFLs and subsequent analysis of terminus position changes, and iceberg calving rates on FRIS, presented in this study, demonstrate the usability of swath elevation data for effectively, and continuously mapping the complete ice front position on one of the largest ice shelves in Antarctica. Compared with conventional CFL mapping techniques, such as by manual delineation using SAR or optical imagery, the elevation-edge method has several advantages and drawbacks to be noted.

Firstly, this new approach applies a single technique using data from only one sensor, with minimal manual intervention, which ensures a consistent data product that is not biased by subjective judgements. This facilitates the assessment of ice front migration by avoiding the need to merge different data sets derived by different techniques with different respective accuracies, therefore avoiding systematic offsets and image artefacts. As the ice shelf cliff height during the year or between

different years is, arguably, less variable than radar backscatter and solar reflectance the method requires less manual intervention or post-processing making it more robust and easier to automate. Secondly the CryoSat-2 altimetry record runs, at time of writing, into its 10th year of mission operations and thus provides an extensive relatively long-term systematic record with short and regular mapping intervals, that permits study of sub-annual and longer term (inter-)annual variation for the first time. Thirdly, the high latitudinal limit of the CryoSat-2 data coverage is Antarctic-wide, with complete coverage over all known ice shelf calving fronts across the continent, providing an opportunity to derive regular calving front locations for ice shelves around Antarctica. Finally, the use of elevation data allows to simultaneously derive ice cliff position, height, thickness and calving volume, which is advantageous for estimating the total freshwater flux.

The principal weakness of the altimetry derived elevation-edge technique is its lower spatial resolution source data (DEMs) in comparison with higher resolution optical or SAR images (5 to 10 m) used for manual CFL mapping. In this study, we used a grid spacing of 200 m which is near the limit for the biannual DEMs based on the data density of CryoSat-2 swath data. Nevertheless, this is of a similar magnitude as MODIS data used for continent-wide coastline mapping [21] and justified as the ice shelf is mostly relatively simple and flat terrain. The lower temporal resolution causes the ice edge to become blurred as changes occurring in the 6-month epochs are averaged. The use of a Lagrangian framework, as done in elevation change studies to remove this effect (for example, [35]), would change the calving front position which is not desirable. The lower spatial resolution of our new technique might limit the applicability of it on smaller outlet glaciers and ice shelves, such as those on the Antarctic Peninsula. These glaciers are often situated in narrow fjords, which can be complex terrain for satellite altimetry [48]. As is the case when using imagery, complex calving fronts with many fractures and/or icebergs/ice-melange require additional manual post-processing. Overall, the dramatically reduced time required to calculate the calving front for nearly a decade on the FRIS, vastly outweighs the stated limitations, making it possible for us to evaluate the validity of the steady-state calving approach, which has been the default 'modelled' method for all historical studies.

5. Conclusions

In this study, we have demonstrated the capability of CryoSat-2 radar altimetry data to map CFL and calving front migration of ice shelves, with a height of a several tens of meters, using time series of gridded elevation data from swath processing. We demonstrated the feasibility of the approach by deriving a unique data set of ice front positions for the Filchner-Ronne Ice Shelf between 2012 and 2018. Our results compare to within two to three pixels compared to manually derived ice front positions from Sentinel-1 SAR imagery and reveal an overall gradual advance of the entire ice front, interrupted only by a calving event on FIL in 2012/13 and several smaller-scale events. By combining our CFLs with ice velocity measurements from Sentinel-1 and ice thickness, we used this new data set to calculate area change and iceberg calving rates. We found that the Filchner-Ronne Ice Shelf is currently growing at a rate exceeding 800 km² per year. Along flowlines, we measure an advance rate between 0.4 and 1.7 km a⁻¹ and calculated calving rates of 7 ± 1 Gt a⁻¹ and 9 ± 1 Gt a⁻¹ for RON and FIL, respectively. This is of an order of magnitude less than their steady-state calving fluxes.

The novel elevation-edge approach outlined in this study is complementary to standard CFL detection methods. Although with its limitations regarding spatial resolution and applicability in 'difficult' terrain it has the potential to be applied for derivation of a homogeneous and regular sub-annual circum-Antarctic record based on one single sensor and uninterrupted for the CryoSat-2 mission lifespan. To our knowledge there is no other sensor or approach that is capable of this. Moreover, it enables existing gaps to be filled in regions and during periods with no or few observations from other sensors. The ability to derive of both CFL and ice thickness simultaneously from a single platform is another clear benefit facilitating applications such as iceberg calving rate and ice shelf mass balance calculations.

This new application of CryoSat-2, outlined in this article, will greatly benefit the investigations of environmental forcing on ice flow and terminus dynamics by providing accurate calving front locations and improved constraints for calving models. With the extension of the CryoSat-2 mission, this provides excellent opportunity for satellite radar altimetry to derive valuable new CFL data sets for monitoring climate change impacts in Antarctica.

Author Contributions: J.W. and T.N. initiated and designed the outline of the study; J.W. developed and implemented the methodology for CFL extraction from CryoSat-2 swath altimetry; J.W. analyzed the data, interpreted the results and wrote the article with contributions from all co-authors; N.G. processed the CryoSat-2 swath data and leads the CryoTop Evolution and CryoSat+ CryoTop projects; A.E.H., N.G., M.J.E. and M.R.D. provided useful comments and reviewed the manuscript.

Funding: This work was supported by European Space Agency (ESA) contracts including Support to Science Elements (STSE) CryoSat+ CryoTop 4000107394/12/I-NB and CryoTop Evolution 4000116874/16/I-NB (NG). A.H. was also funded by a NERC Fellowship (NE/R012407/1).

Acknowledgments: The authors wish to thank the European Space Agency (ESA) for providing open access to CryoSat-2 and Copernicus Sentinel-1 data. J.W., T.N. and A.E.H. acknowledge support from ESA through the STSE and CCI programs. We thank Stefan Ligtenberg for providing the RACMO2/Ant FirnAir content.

Conflicts of Interest: The authors declare no conflict of interest.

Data Availability: All datasets generated and analyzed during the current study are available online. The CFL shapefiles and ice velocity data from Copernicus Sentinel-1 are available from ENVEO's Cryoportale website: <http://cryoportale.enveo.at>. The swath elevation products are available from the UK Polar Data Centre: <https://data.bas.ac.uk/metadata.php?id=GB/NERC/BAS/PDC/01136>.

References

1. Depoorter, M.A.; Bamber, J.L.; Griggs, J.A.; Lenaerts, J.T.M.; Ligtenberg, S.R.M.; Van den Broeke, M.R.; Moholdt, G. Calving fluxes and basal melt rates of Antarctic ice shelves. *Nature* **2013**, *502*, 89–92. [[CrossRef](#)] [[PubMed](#)]
2. Rignot, E.; Jacobs, S.S.; Mouginot, J.; Scheuchl, B. Ice-shelf melting around Antarctica. *Science* **2013**, *341*, 266–270. [[CrossRef](#)] [[PubMed](#)]
3. Lazzara, M.A.; Jezek, K.C.; Scambos, T.A.; MacAyeal, D.R.; Van der Veen, C.J. On the recent calving of icebergs from the Ross Ice Shelf. *Polar Geogr.* **1999**, *23*, 201–212. [[CrossRef](#)]
4. Hogg, A.E.; Gudmundsson, G.H. Impacts of the Larsen-C Ice Shelf calving event. *Nat. Clim. Chang.* **2017**, *7*, 540. [[CrossRef](#)]
5. Rott, H.; Skvarca, P.; Nagler, T. Rapid collapse of Northern Larsen Ice Shelf, Antarctica. *Science* **1996**, *271*, 788–792. [[CrossRef](#)]
6. Rack, W.; Rott, H. Pattern of retreat and disintegration of Larsen B Ice Shelf, Antarctic Peninsula. *Ann. Glaciol.* **2004**, *39*, 505–510. [[CrossRef](#)]
7. Glasser, N.F.; Scambos, T.A. A structural glaciological analysis of the 2002 Larsen B ice-shelf collapse. *J. Glaciol.* **2008**, *54*, 3–16. [[CrossRef](#)]
8. Rott, H.; Rack, W.; Skvarca, P.; De Angelis, H. Northern Larsen Ice Shelf, Antarctica: Further retreat after collapse. *Ann. Glaciol.* **2002**, *34*, 277–282. [[CrossRef](#)]
9. De Angelis, H.; Skvarca, P. Glacier surge after ice shelf collapse. *Science* **2003**, *299*, 1560–1562. [[CrossRef](#)]
10. Scambos, T.A.; Bohlander, J.A.; Shuman, C.A.; Skvarca, P. Glacier acceleration and thinning after ice shelf collapse in the Larsen B embayment, Antarctica. *Geophys. Res. Lett.* **2004**, *31*, L18402. [[CrossRef](#)]
11. Scambos, T.A.; Berthier, E.; Shuman, C.A. The triggering of subglacial lake drainage during rapid glacier drawdown: Crane Glacier, Antarctic Peninsula. *Ann. Glaciol.* **2011**, *52*, 74–82. [[CrossRef](#)]
12. Favier, L.; Pattyn, F.; Berger, S.; Drews, R. Dynamic influence of pinning points on marine ice-sheet stability: A numerical study in Dronning Maud Land, East Antarctica. *Cryosphere* **2016**, *10*, 2623–2635. [[CrossRef](#)]
13. Fürst, J.J.; Durand, G.; Gillet-Chaulet, F.; Tavard, L.; Rankl, M.; Braun, M.; Gagliardini, O. The safety band of Antarctic ice shelves. *Nat. Clim. Chang.* **2016**, *6*, 479–482. [[CrossRef](#)]
14. Baumhoer, C.A.; Dietz, A.J.; Dech, S.; Kuenzer, C. Remote Sensing of Antarctic Glacier and Ice-Shelf Front Dynamics—A Review. *Remote Sens.* **2018**, *10*, 1445. [[CrossRef](#)]

15. Mottram, R.; Simonsen, S.B.; Svendsen, S.H.; Barletta, V.R.; Sandberg Sørensen, L.; Nagler, T.; Wuite, J.; Groh, A.; Horwath, M.; Rosier, J.; et al. An integrated view of Greenland Ice Sheet mass changes based on models and satellite observations. *Remote Sens.* **2019**, *11*, 1407. [CrossRef]
16. Krieger, L.; Floricioiu, D. Automatic glacier calving front delineation on TerraSAR-X and Sentinel-1 SAR imagery. In Proceedings of the 2017 IEEE International Geoscience and Remote Sensing Symposium (IGARSS), Fort Worth, TX, USA, 23–28 July 2017; pp. 2817–2820. [CrossRef]
17. Mohajerani, Y.; Wood, M.; Velicogna, I.; Rignot, E. Detection of Glacier Calving Margins with Convolutional Neural Networks: A Case Study. *Remote Sens.* **2019**, *11*, 74. [CrossRef]
18. Liu, H.; Jezek, K.C. A Complete High-Resolution Coastline of Antarctica Extracted from Orthorectified Radarsat Sar Imagery. *Photogramm. Eng. Remote Sens.* **2004**, *70*, 605–616. [CrossRef]
19. Liu, H.; Jezek, K.C. Automated extraction of coastline from satellite imagery by integrating Canny edge detection and locally adaptive thresholding methods. *Int. J. Remote Sens.* **2004**, *25*, 937–958. [CrossRef]
20. Jezek, K.C. RADARSAT-1 Antarctic Mapping Project: Change-detection and surface velocity campaign. *Ann. Glaciol.* **2002**, *34*, 263–268. [CrossRef]
21. Scambos, T.A.; Haran, T.M.; Fahnestock, M.A.; Painter, T.H.; Bohlander, J. MODIS-based Mosaic of Antarctica (MOA) data sets: Continent-wide surface morphology and snow grain size. *Remote Sens. Environ.* **2007**, *111*, 242–257. [CrossRef]
22. Fricker, H.A.; Young, N.W.; Allison, I.; Coleman, R. Iceberg calving from the Amery Ice Shelf, East Antarctica. *Ann. Glaciol.* **2002**, *34*, 241–246. [CrossRef]
23. Rignot, E. Ice-shelf changes in Pine Island Bay, Antarctica, 1947–2000. *J. Glaciol.* **2002**, *48*, 247–256. [CrossRef]
24. Miles, B.W.J.; Stokes, C.R.; Jamieson, S.S.R. Simultaneous disintegration of outlet glaciers in Porpoise Bay (Wilkes Land), East Antarctica, driven by sea ice break-up. *Cryosphere* **2017**, *11*, 427–442. [CrossRef]
25. Rott, H.; Abdel Jaber, W.; Wuite, J.; Scheiblaue, S.; Floricioiu, D.; Van Wessem, J.M.; Nagler, T.; Miranda, N.; Van den Broeke, M.R. Changing pattern of ice flow and mass balance for glaciers discharging into the Larsen A and B embayments, Antarctic Peninsula, 2011 to 2016. *Cryosphere* **2018**, *12*, 1273–1291. [CrossRef]
26. Gourmelen, N.; Escorihuela, M.J.; Shepherd, A.; Foresta, L.; Muir, A.; Garcia-Mondéjar, A.; Drinkwater, M.R. CryoSat-2 swath interferometric altimetry for mapping ice elevation and elevation change. *Adv. Space Res.* **2018**, *62*, 1226–1242. [CrossRef]
27. Chuter, S.J.; Bamber, J.L. Antarctic ice shelf thickness from CryoSat-2 radar altimetry. *Geophys. Res. Lett.* **2015**, *42*, 10721–10729. [CrossRef]
28. Rosier, S.H.R.; Hofstede, C.; Brisbourne, A.M.; Hattermann, T.; Nicholls, K.W.; Davis, P.E.D.; Anker, P.G.D.; Hillenbrand, C.-D.; Smith, A.M.; Corr, H.F.J. A new bathymetry for the southeastern Filchner-Ronne Ice Shelf: Implications for modern oceanographic processes and glacial history. *J. Geophys. Res. Oceans* **2018**, *123*, 4610–4623. [CrossRef]
29. Hogg, A.E.; Shepherd, A.; Gilbert, L.; Muir, A.; Drinkwater, M.R. Mapping ice sheet grounding lines with CryoSat-2. *Adv. Space Res.* **2018**, *62*, 1191–1202. [CrossRef]
30. Ferrigno, J.G.; Gould, W.G. Substantial changes in the coastline of Antarctica revealed by satellite imagery. *Polar Rec.* **1987**, *23*, 577. [CrossRef]
31. MacAyeal, D.R.; Padman, L.; Drinkwater, M.R.; Fahnestock, M.; Gotis, T.T.; Gray, A.L.; Kerman, B.; Lazzara, M.; Rignot, E.; Scambos, T.; et al. Effects of Rigid Body Collisions and Tide-forced Drift on Large Tabular Icebergs of the Antarctic. 2002. Available online: http://geosci.uchicago.edu/~{}drm7/research/Icebergs_of_Y2k.pdf (accessed on 23 July 2019).
32. Larour, E.; Rignot, E.; Aubry, D. Modelling of rift propagation on Ronne Ice Shelf, Antarctica, and sensitivity to climate change. *Geophys. Res. Lett.* **2004**, *31*, L16404. [CrossRef]
33. Wingham, D.J.; Francis, C.R.; Baker, S.; Bouzinac, C.; Brockley, D.; Cullen, R.; De Chateau-Thierry, P.; Laxona, S.W.; Mallow, U.; Mavrocordatos, C.; et al. CryoSat: A mission to determine the fluctuations in Earth's land and marine ice fields. *Adv. Space Res.* **2006**, *37*, 841–871. [CrossRef]
34. Howat, I.M.; Porter, C.; Smith, B.E.; Noh, M.-J.; Morin, P. The Reference Elevation Model of Antarctica. *Cryosphere* **2019**, *13*, 665–674. [CrossRef]
35. Gourmelen, N.; Goldberg, D.; Snow, K.; Henley, S.; Bingham, R.G.; Kimura, S.; Hogg, A.; Shepherd, A.; Mouginot, J.; Lenaerts, J.T.M.; et al. Channelized melting drives thinning under a rapidly melting Antarctic ice shelf. *Geophys. Res. Lett.* **2017**, *44*, 9796–9804. [CrossRef]

36. Goldberg, D.; Gourmelen, N.; Kimura, S.; Millan, R.; Snow, K. How accurately should we model ice shelf melt rates? *Geophys. Res. Lett.* **2019**, *46*, 189–199. [[CrossRef](#)]
37. Smith, W.H.F.; Wessel, P. Gridding with continuous curvature splines in tension. *Geophysics* **1990**, *55*, 293–305. [[CrossRef](#)]
38. Mayer-Gürr, T.; Pail, R.; Gruber, T.; Fecher, T.; Rexer, M.; Schuh, W.-D.; Kusche, J.; Brockmann, J.-M.; Rieser, D.; Zehentner, N.; et al. The combined satellite gravity field model GOCCO05s. *Geophys. Res. Abstr.* **2015**, *17*, 12364.
39. Canny, J. A computational approach to edge detection. *IEEE Trans. Pattern Anal. Mach. Intell.* **1986**, *8*, 679–698. [[CrossRef](#)]
40. Paterson, W.S.B. *The Physics of Glaciers*, 3rd ed.; Elsevier: Oxford, UK, 1994.
41. Vieli, A.; Funk, M.; Blatter, H. Flow dynamics of tidewater glaciers: A numerical modelling approach. *J. Glaciol.* **2001**, *47*, 595–606. [[CrossRef](#)]
42. Liu, Y.; Moore, J.C.; Cheng, X.; Gladstone, R.M.; Bassis, J.N.; Liu, H.; Wen, J.; Hui, F. Ocean-driven thinning enhances iceberg calving and retreat of Antarctic ice shelves. *Proc. Natl. Acad. Sci. USA* **2015**, *112*, 3263–3268. [[CrossRef](#)]
43. Nagler, T.; Rott, H.; Hetzenecker, M.; Wuite, J.; Potin, P. The Sentinel-1 Mission: New Opportunities for Ice Sheet Observations. *Remote Sens.* **2015**, *7*, 9371–9389. [[CrossRef](#)]
44. Ligtenberg, S.R.M.; Kuipers-Munneke, P.; Van den Broeke, M.R. Present and future variations in Antarctic firn air content. *Cryosphere* **2014**, *8*, 1711–1723. [[CrossRef](#)]
45. Van den Broeke, M.; Van de Berg, W.; Van Meijgaard, E. Firn depth correction along the Antarctic grounding line. *Antarct. Sci.* **2008**, *20*, 513–517. [[CrossRef](#)]
46. The IMBIE Team. Mass balance of the Antarctic Ice Sheet from 1992 to 2017. *Nature* **2018**, *558*, 219–222. [[CrossRef](#)] [[PubMed](#)]
47. IPCC. Summary for Policymakers. In *IPCC Special Report on the Ocean and Cryosphere in A Changing Climate*; Pörtner, H.-O., Roberts, D.C., Masson-Delmotte, V., Zhai, P., Tignor, M., Poloczanska, E., Mintenbeck, K., Nicolai, M., Okem, A., Petzold, J., et al., Eds.; 2019; In press.
48. Dehecq, A.; Gourmelen, N.; Shepherd, A.; Cullen, R.; Trouvé, E. Evaluation of CryoSat-2 for height retrieval over the Himalayan range. In Proceedings of the CryoSat-2 Third User Workshop, Dresden, Germany, 12–14 March 2013.



© 2019 by the authors. Licensee MDPI, Basel, Switzerland. This article is an open access article distributed under the terms and conditions of the Creative Commons Attribution (CC BY) license (<http://creativecommons.org/licenses/by/4.0/>).